Highly conductive and stretchable nanostructured ionogels for 3D printing capacitive sensors with superior performance

Xiangnan He[1,2], Biao Zhang [3], Qingjiang Liu[1,2], Hao Chen[1,2], Jianxiang Cheng[1,2], Bingcong Jian [1,2], Hanlin Yin[1,2], Honggeng Li[1,2], Ke Duan [4], Jianwei Zhang[4] & Qi Ge [1,2] ✉

Ionogels are promising material candidates for ionotronics due to their excellent ionic conductivity, stretchability, and thermal stability. However, it is challenging to develop 3D printable ionogels with both excellent electrical and mechanical properties. Here, we report a highly conductive and stretchable nanostructured (CSN) ionogel for 3D printing ionotronic sensors. We propose the photopolymerization-induced microphase separation strategy to prepare the CSN ionogels comprising continuous conducting nanochannels intertwined with cross-linked polymeric framework. The resultant CSN ionogels simultaneously achieves high ionic conductivity (over 3 S m^{-1}), high stretchability (over 1500%), low degree of hysteresis (0.4% at 50% strain), wide-temperature-range thermostability (−72 to 250 °C). Moreover, its high compatible with DLP 3D printing enables the fabrication of complex ionogel micro-architectures with high resolution (up to 5 μm), which allows us to manufacture capacitive sensors with superior sensing performances. The proposed CSN ionogel paves an efficient way to manufacture the next-generation capacitive sensors with enhanced performance.

Ionotronics are a family of devices functioning by a hybrid circuit of mobile ions and mobile electrons. The rapid advancement of stretchable ionic conductors allows ionotronics to be employed in various applications including artificial skins[1], muscles[2], axons[3], ionic touchpads[4], stretchable ionotronic luminescence[5], and many others[6–8]. To date, stretchable ionic conductors mainly include hydrogels[9], ionic conductive elastomers[10], and ionogels[11]. Hydrogel is a hydrophilic polymer network containing a large amount of water, and its high conductivity can be obtained by adding inorganic[12] or even organic salts[13]. However, dehydration of hydrogels in dry environment becomes a critical challenge for the hydrogel-based ionotronic devices[9]. Ionic conductive elastomers (ICEs) are the elastomers incorporated with organic salts which are primarily lithium salts. The solvent-free nature lets ICEs avoid the dehydration issue, but suffer from poor ionic conductivity (10^{-5} ~ 10^{-2} S·m^{-1}) due to the low mobility of ions. Moreover, lithium salts make ICEs quickly absorb a large amount of moisture in the air, which causes unstable performances of the ICE-based ionotronic devices in terms of conductivity and transparency[14]. Different from hydrogels and ICEs, ionogels are the polymer networks swollen with ionic liquid (IL) which are room-

[1]Shenzhen Key Laboratory of Soft Mechanics & Smart Manufacturing, Southern University of Science and Technology, Shenzhen, China. [2]Department of Mechanical and Energy Engineering, Southern University of Science and Technology, 518055 Shenzhen, China. [3]Xi'an Institute of Flexible Electronics, Northwestern Polytechnical University, 127 West Youyi Road, Xi'an, China. [4]Department of Materials Science and Engineering, College of Aerospace Science and Engineering, National University of Defense Technology, Changsha, China. ✉e-mail: geq@sustech.edu.cn

temperature molten salts consisting of cations and anions. Due to the unique features such as nonvolatility, high thermal and electrochemical stability, excellent ionic conductivity, and nonflammability, ionogels have been widely used to form stretchable ionotronic devices, especially ionotronic sensors[7,15].

Manufacturing micro-architectures of ionogels is a necessary step to enable ionogel-based ionotronic sensors to have extraordinary performance and functionality such as ultra-broad range high sensitivity[16] and high linearity[17], multi-mode perception[18], texture recognition[19], motion-interference-free sensing[20], and others[21,22]. However, the current method to achieve micro-architectures mainly relies on molding, which is a time-consuming process involving multiple steps and limits the geometric complexity of manufactured micro-architectures. Three-dimensional (3D) printing that creates complex 3D objects in free forms is considered as an efficient approach to endow ionogel with complex micro-architectures. In recent years, the extrusion-based direct ink writing (DIW) technology has been widely adopted for 3D printing ionogels[23,24]. Compared to DIW, digital light processing (DLP) 3D printing is more competent to fabricate 3D structure with refined and complex micro-architectures as it creates 3D objects by digitalized photopolymerization[25,26]. However, despite a few recent explorations on developing UV curable ionogels, currently, DLP 3D printed ionogel sensors exhibit neither high resolution nor remarkable sensing capabilities[27–33] (Table S1). Attempts to achieve high ionic conductivity by increasing the IL contents substantially compress the printability and mechanical properties of those UV curable ionogels.

Here, we report an UV curable ionogel with bicontinuous nanostructures to achieve high conductivity without sacrificing its printability and mechanical properties. We propose a photopolymerization-induced microphase separation strategy to prepare the highly conductive and stretchable nanostructured (CSN) ionogels comprising continuous conducting nanochannels intertwined with cross-linked polymeric framework. The resultant CSN ionogels simultaneously achieves high ionic conductivity (over 3 S m^{-1}), high stretchability (over 1500%), low degree of hysteresis (degree of hysteresis: 0.4% at 50% strain), wide-temperature-range thermostability (−72 to 250 °C), and humidity tolerance. More importantly, its high compatibility with DLP 3D printing allows us to fabricate complex ionogel micro-architectures with high resolution (up to 5 μm). Exploiting such high printability, we can manufacture electron double layer (EDL) - based capacitive sensors by rationally designing the geometries of the CSN ionogel layers to achieve superior sensing performances such as high sensitivity, high linearity, fast dynamic response, excellent cyclic stability, and wide operating temperature range. To demonstrate these superior performances, we use the sensor to monitor real-time physiological signals including deep breath, swallow, and pulsation. Furthermore, we integrate the sensors to a robotic gripper that can detect signals in a wide temperature range and perceive different combinations of signals while grasping various objects. We further use the CSN ionogel-based EDL capacitive sensors to form a pressure sensor array for high resolution pressure mapping. The proposed CSN ionogel paves an efficient way to fabricate micro-structured ionogels which potentially can be used to manufacture the next generation of capacitive sensors with enhanced performance.

Results

Fabrication and characterization of CSN ionogels

Figure 1a presents the chemicals used to prepare the ultraviolet (UV) curable thus 3D printable CSN ionogel precursor solution that consists of benzyl acrylate (BA) as monomer, small amount of poly(ethylene glycol) diacrylate (PEGDA) as crosslinker, 2,4,6-trimethylbenzoyl diphenylphosphine oxide (TPO) as photoinitiator, ionic liquid (IL) 1-ethyl-3-methylimidazolium dicyanamide ([EMIm][DCA]). More importantly, poly(ethylene glycol) methyl ether methacrylate (PEGMA) is added to avoid the macroscopic phase separation between polymer

network and IL during photopolymerization. Figure 1b–d illustrates the photopolymerization process of a CSN ionogel. Irradiation of UV light activates the TPO photoinitiator to generate free radicals that propagate through BA, PEGMA, and PEGDA molecules (Fig. 1b) which are chemically crosslinked to form covalent networks (Fig. 1c) where the detailed chemical structure is presented in Fig. 1d. Details on preparing the CSN ionogel precursor solution can be found in Materials and Methods.

To achieve the CSN ionogel where the IL is uniformly distributed in the polymer network, PEGMA plays the key role. To demonstrate the effect of PEGMA content on physical properties of the ionogels, as shown in Fig. 1e and Fig.S1, we prepare a series of ionogels with different BA:PEGMA ratios. Detailed compositions of these ionogels are shown in Table S2. Although the [EMIm][DCA] is well mixed in the BA (BA:PEGMA = 10:0) precursor solution, photopolymerization turns the ionogel to be translucent with low transmittance (~ 70%, details can be found in Fig. S2a and Fig. S3) due to the emergence of substantial white plaques resulted from the macroscopic phase separation (Fig. 1f). This can be explained by the change of free energy of mixing ΔF_{mix} ($\Delta F_{mix} = \Delta U_{mix}$ - $T\Delta S_{mix}$, where ΔU_{mix} is enthalpy change, ΔS_{mix} is entropy change, and T is absolute temperature)[34]. ΔF_{mix} needs to be negative when the two species are miscible. Photopolymerization converts the BA solution to polymer network which greatly decreases the mixing entropy ΔS_{mix} of the polymer-IL system so that ΔF_{mix} increases and phase separation occurs. The variation of ΔF_{mix} during photopolymerization is discussed in Eq. (S1) of Supplementary Materials. By adding PEGMA into the polymer network, the ionogel gradually turns to be transparent. When BA:PEGMA is less than 7:3, the transmittance is greater than 90% (Fig. S3), and no phase separation is observed (inset photographs in Fig. 1e). Compared with the BA polymer network, no macroscopic phase separation can be observed in the ionogel consisting of BA-PEGMA polymer network and IL (Fig. 1g and Fig. S2b). This is because the introduction of PEGMA grafts polyethylene oxide (PEO) side chains to the polymer network which facilitates the interaction between polymer network and IL[35], and reduces the mixing enthalpy (ΔU_{mix}) as well as ΔF_{mix}. The variation of ΔU_{mix} after adding PEGMA is discussed in Eq. (S2) of Supplementary Materials. The interaction between polymer network and IL can be validated by Fourier transform infrared (FTIR) spectroscopy. As shown in Fig. S4, the increase in the PEGMA content shifts the C≡N group stretching and C-N group stretching of [EMIm][DCA] to a lower wavenumber due to the interaction between PEO side chains of PEGMA and IL molecules.

Besides the optical property, the electrical conductivity is also significantly influenced by the PEGMA content. Figure 1e shows that the conductivity increases from 4.8×10^{-4} S m^{-1} to 0.11 S m^{-1} by changing the BA:PEGMA ratio from 10:0 to 6:4. The high conductivity of the BA-PEGMA ionogel can be attributed to the bicontinuous nanostructure comprising interpenetrating domains of BA phase and PEGMA phase (Fig. 1h) resulted from photopolymerization-induced microphase separation[36,37]. Once the amount of PEGMA is sufficient, the PEO side chains from PEGMA form continuous microchannels percolating in the polymer network which highly facilitate ion transportation (Fig. 1i). To verify the existence of the bicontinuous morphology resulted from the introduction of PEGMA, we perform small-angle X-ray scattering (SAXS) experiments on both BA and BA-PEGMA ionogels. Figure 1j shows that the scattering patterns for both samples are circular indicating that the polymer chains are randomly oriented. In Fig. 1k, the SAXS scattering intensity profile of the BA-PEGMA ionogel shows a single broad scattering peak (the magnitude of the scattering vector q ranging from 0.041 to 1.22 nm with the peak point $q^* = 0.1$ nm^{-1}) indicating the nanostructured morphology resulted from the microphase separation. Based on d-q relation ($d = 2\pi/q$)[35,37], the feature size d of nanostructure ranges from 5 to 153 nm. In contrast, the SAXS profile of the BA ionogel shows no peak indicating no nanostructure existing in the BA ionogel. The bicontinuous nanostructure of
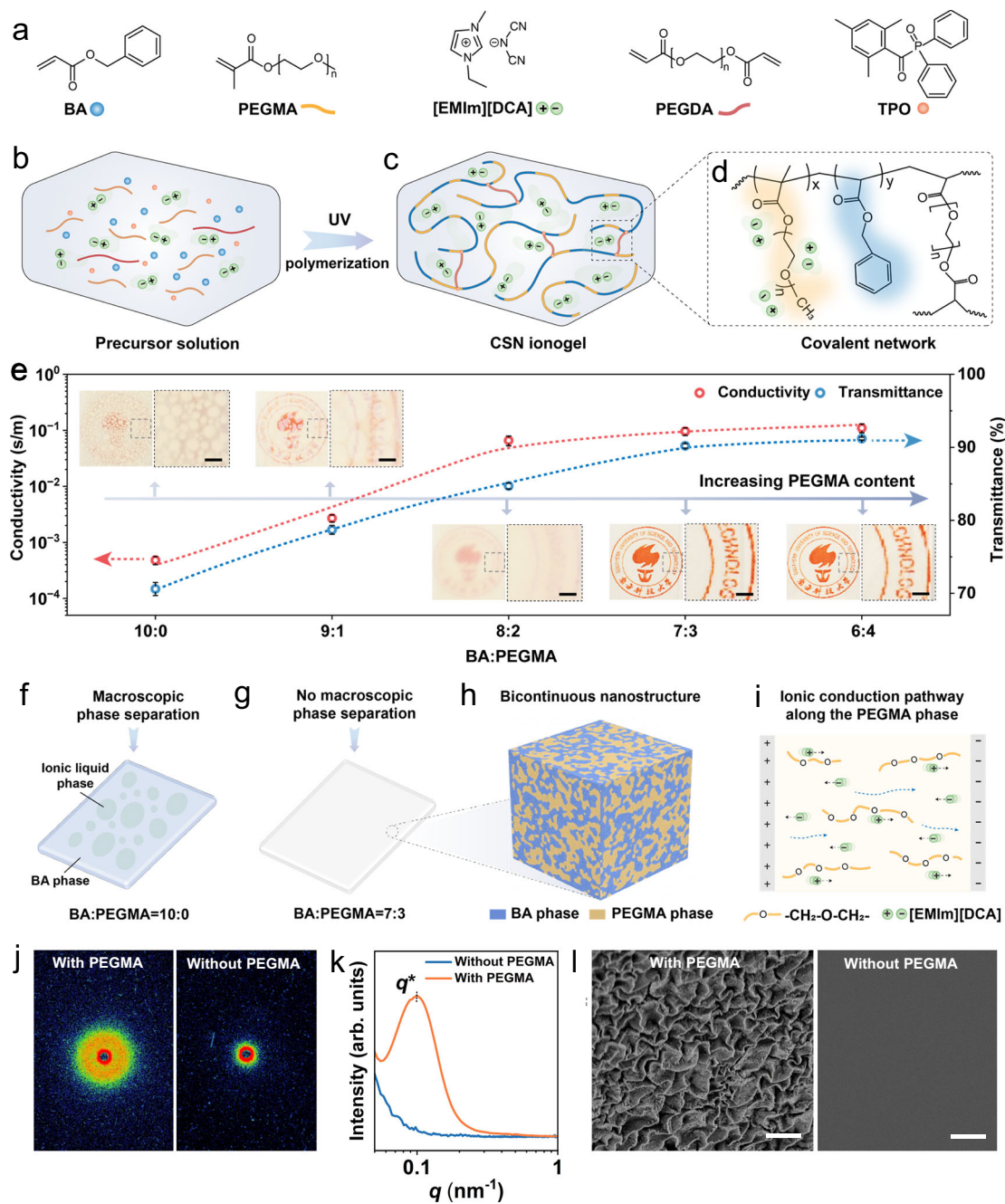
Fig. 1 | Synthesis and characterizations of CSN ionogels. a Detailed chemical structures of BA, PEGMA, [EMIm][DCA], PEGDA and TPO that are used to prepare CSN ionogels precursor solution. **b–d** Illustrations of the photopolymerization process during photopolymerization. **b** CSN ionogels precursor solution before photopolymerization. **c** CSN ionogels network structure after photopolymerization. **d** Detailed chemical structure of crosslinked CSN ionogels. **e** Comparison on conductivity and transmittance of the ionogels with different PEGMA contents. Scale bar in inset photographs: 1 mm. **f** Illustration of macroscopic phase separation resulted from photopolymerizing the pure BA ionogel (BA:PEGMA = 0). **g** Illustration of ionogel with no macroscopic phase separation resulted from photopolymerizing the BA-PEGMA ionogel precursor with BA:PEGMA ratio of 7:3. **h** Illustration of the microphase-separated structure within the BA-PEGMA ionogel. **i** Schematic presentation of ionic pathway along the PEGMA phase. **j**, **k** 2D SAXS scattering patterns (**j**) and SAXS scattering intensity variation (**k**) for ionogel with/without PEGMA. **l** SEM images for the ionogels with/without PEGMA. Scale bar: 1 μm. Data are presented as the mean values ± SD, $n = 3$ independent samples. Source data are provided as a Source Data file.

the BA-PEGMA ionogel is further confirmed by scanning electron microscopy (SEM) image where the bright regions represent the domains of BA phase (Fig. 1l). In contrast, no nanostructured morphology is observed in the SEM image of the BA ionogel. Details on the SAXS and SEM characterizations can be found in Materials and Methods. Moreover, the conductivity of the BA-PEGMA ionogel can be increased by choosing higher molecular weight (M_n) PEGMA while keeping its molar ratio constant (Fig. S5 and Table S3), which further

implies that the PEO side chains from PEGMA do promote ion transportation. In the following work, the CSN ionogels are prepared by choosing the BA:PEGMA ratio of 7:3 and PEGMA M_n of 950 g/mol unless otherwise specified.

Thermomechanical and electrical properties of the CSN ionogel
The content of [EMIm][DCA] IL greatly affects the mechanical and electrical properties of the CSN ionogels. As presented in Fig. 2a and

summarized in Fig. 2b, the increase in the [EMIm][DCA] content from 10 to 70 wt.% results in a rise of the elongation at break from 580 to 1540% but a gradual decrease in Young's modulus from 136 to 12 kPa. In addition, Fig.S6 presents the compressive tests for the ionogels with different [EMIm][DCA] contents: all the ionogel samples exhibit excellent compressibility and can be compressed by 90% without breaking; the stiffness of ionogel decreases with the increase in [EMIm][DCA] content. Detailed compositions of the CSN ionogels with different [EMIm][DCA] contents are shown in Table S4. As shown in Fig. 2c, the conductivity of the CSN ionogel raises from 0.11 to 3.23 S·m⁻¹ by increasing the [EMIm][DCA] content from 10 to 70 wt.%. Moreover, although the ionic conductivity can be achieved by incorporating various ILs or even salts into the polymer network (details can be found in Table S5 and Fig. S7), the resulted conductivity may vary greatly. As compared in Fig. 2d, at the same weight percentage (20 wt.%), the BA-PEGMA polymer with [EMIm][DCA] has the highest conductivity (0.33 S m⁻¹). In contrast, the conductivity of the BA-PEGMA polymer with [BVIm][BF$_4$] or [BVIm][TFSI] is about a few 1×10^{-4} S·m⁻¹ as the [BVIm] cations are engrafted to polymer network through photopolymerization and only the anions are mobile; the conductivity of the ionogels with [EMIm][TFSI] or [EMIm][OTF] is also lower (0.006 S m⁻¹ or 0.05 S m⁻¹) as the anions are larger and less mobile than [DCA][38]. Moreover, compared to the polymer incorporated with [EMIm]-based IL, the one with organic salt LiTFSI which has been used as ionic source exhibits much lower conductivity (1.4×10^{-3} S m⁻¹) due to the solid-state nature of LiTFSI. To demonstrate the high conductivity of the ionogel with [EMIm][DCA], as shown in Fig. 2e, in a parallel circuit where a 150 V AC (1000 Hz) voltage is applied, three mini light-emitting diode (LED) dots can be lighted up in the component where the ionogel with [EMIm][DCA] is used as conductor; in comparison, the component with the LiTFSI-based conductor fails to light the LED dots due to its low conductivity. In fact, as summarized in Fig. 2f, the high conductivity of CSN ionogel surpasses the previously reported ionic conductive and stretchable materials (details can be seen in Table S1). In particular, the CSN ionogel with 70 wt.% [EMIm][DCA] exhibits high ionic conductivity (3.23 S m⁻¹) which is at least one order of magnitude higher than that of previously reported ionogels[11,27–29,31–33,39–48].

For making high-performance ionic sensors, the ionogels are also required to have high elasticity and low hysteresis to ensure good stability and repeatability of detected signals. As shown in Fig. 2b, c, compared with the CSN ionogel with 70 wt.% [EMIm][DCA], the one with 40 wt.% [EMIm][DCA] has higher Young's modulus (63 kPa) and reasonable high ionic conductivity (0.86 S m⁻¹) which are both favorable properties for ionic sensors. As shown in Fig. 2g and Fig. S8, the residual strain of the CSN ionogel can be reduced from 24.6% to 2.9% under a 100% cyclic strain by increasing the PEGDA crosslinker from 0.2 to 2 wt.%. Detailed compositions of the CSN ionogels with different PEGDA contents are shown in Table S6. Nevertheless, the stretchability of the CSN ionogel is traded off, and decreases from 610% to 120% as the increase in crosslinking density leads to the decrease in the average length of linear chains between crosslinking points (illustrative inset in Fig. 2g). Figure 2h shows that the residual strain becomes lower when the maximum strain of the loading cycle decreases. The hysteresis is negligible when the maximum strain is less than 50%. Figure 2i presents the relative change in resistive signal of the CSN ionogel during a cyclic loading of 50% strain where the loading signal perfectly overlaps the unloading one. We can calculate the degree of hysteresis (DH) as $DH = (A_{Loading} - A_{Unloading}) \cdot A_{Loading}^{-1} \times 100\%$, where $A_{Loading}$ and $A_{Unloading}$ are the areas under the loading and unloading curves, respectively[49]. The DH value of the CSN ionogel is about 0.4% at 50% strain. The low hysteresis endows the CSN ionogel-based strain sensor with excellent stability and repeatability which are confirmed by the step-up/step-down loading test (Fig. S9a), the cyclic loading test of gradually increased maximum strain (Fig. S9b), and the 1000 cycles of

cyclic test at the maximum strain of 50% (Fig. S9c). In the following work, the content of PEGDA of CSN ionogels is 2 wt.% unless otherwise specified.

More importantly, the CSN ionogels exhibit excellent stability in a wide temperature range and humid environment. Figure 2j and Fig. S10 present the dynamic mechanical analysis (DMA) results which indicate the glass transition temperature (T_g) of the CSN ionogels decreases with the increase in the IL content. When the IL content is 30 wt.%, the T_g of the ionogel reaches −57 °C; when the IL content is further increased to 70 wt.%, the T_g can even drop to −72 °C. The low T_g ensures the functioning of the CSN ionogels at low temperature environment. Moreover, we perform the thermogravimetric analyses (TGA) to examine the stability of the CSN ionogels at high temperature environment. The TGA curves in Fig. 2k show that no apparent weight loss is observed when temperature is lower than 250 °C. Figure 2j, k confirm that the CSN ionogels can function within an ultra-wide operating temperature range. As shown in Fig. S11, after 24 h at 100 °C or −30 °C, there is no change in the weight and morphology of the ionogel samples. More importantly, compared to the ionic conductors with LiTFSI, the CSN ionogels exhibit good stability in humid environment. As shown in Fig. 2l and Fig. S12, we place the ionogel and the LiTFSI-based conductor in a humid environment (relative humidity: 80%) for 7 days and compare the weight variations. No weight change has been observed on the ionogel sample over the 7 days; in contrast, the ionic conductor with LiTFSI absorbs moisture from the air, resulting in an ~20% increase in the weight. In fact, absorbing a large amount of moisture also significantly changes sample's transparency. As demonstrated in the insets of Fig. 2l, after being placed in the humid environment for 1 h, the LiTFSI-based conductor turns to be translucent, while the transparency of the CSN ionogel remains unchanged. The excellent stability of CSN ionogels in humid environment can be attributed to two reasons: compared with LiTFSI, the ILs are much less hydroscopic[42,50]; the hydrophobic domains of the BA phase further enhance the stability of the CSN ionogels in humid environment.

3D printing CSN ionogels

Owing to low viscosity and high photo-reactivity, the CSN ionogels are highly suitable for DLP 3D printing to create ionotronic devices with refined features and complex geometries. As shown in Fig. 3a, the room-temperature viscosities of the CSN ionogel precursor solutions with different [EMIm][DCA] contents ranging from 10 to 70 wt.% are all less than 0.06 Pa s which is sufficiently low for DLP 3D printing[26]. In Fig. 3b, we perform in-situ photo-rheological characterizations to investigate the photo-reactivity of the CSN ionogel precursor solutions. We identify the time to gel point (gelation time) when the storage modulus curve intersects to the loss modulus curve. To cure a 200 μm thick layer of the ionogel with 10 wt.% [EMIm][DCA], the gelation time is ~13 s, and the required unit energy is ~110 mJ cm⁻². As summarized in Fig. 3c (see details in Fig. S13), the gelation time and required unit energy increase when the CSN ionogel contains more [EMIm][DCA]. Overall, when the [EMIm][DCA] content is less than 40 wt.%, the gelation time is less than 30 s which is acceptable for DLP 3D printing. In the following work, we print ionic conductive structures by using the CSN ionogel precursor solution with 40 wt.% [EMIm][DCA] which ensures high printability and conductivity.

As demonstrated in Fig. 3d, the CSN ionogel can be used to print straight lines with ultra-thin horizontal width (up to 5 μm). As shown in Fig. S14, by precisely controlling the energy dosage of exposed UV light, the vertical curing depth for the CSN ionogel can be optimized to be 20 μm. The high compatibility with DLP 3D printing allows us to use CSN ionogels to print highly complex geometries with high resolution, which is reflected by the printed Gyroid structure with a wall thickness of ~50 μm (Fig. 3e), Kelvin foam structure, and Octet truss lattice structure (Fig. S15). Compared to the previous works on 3D printing
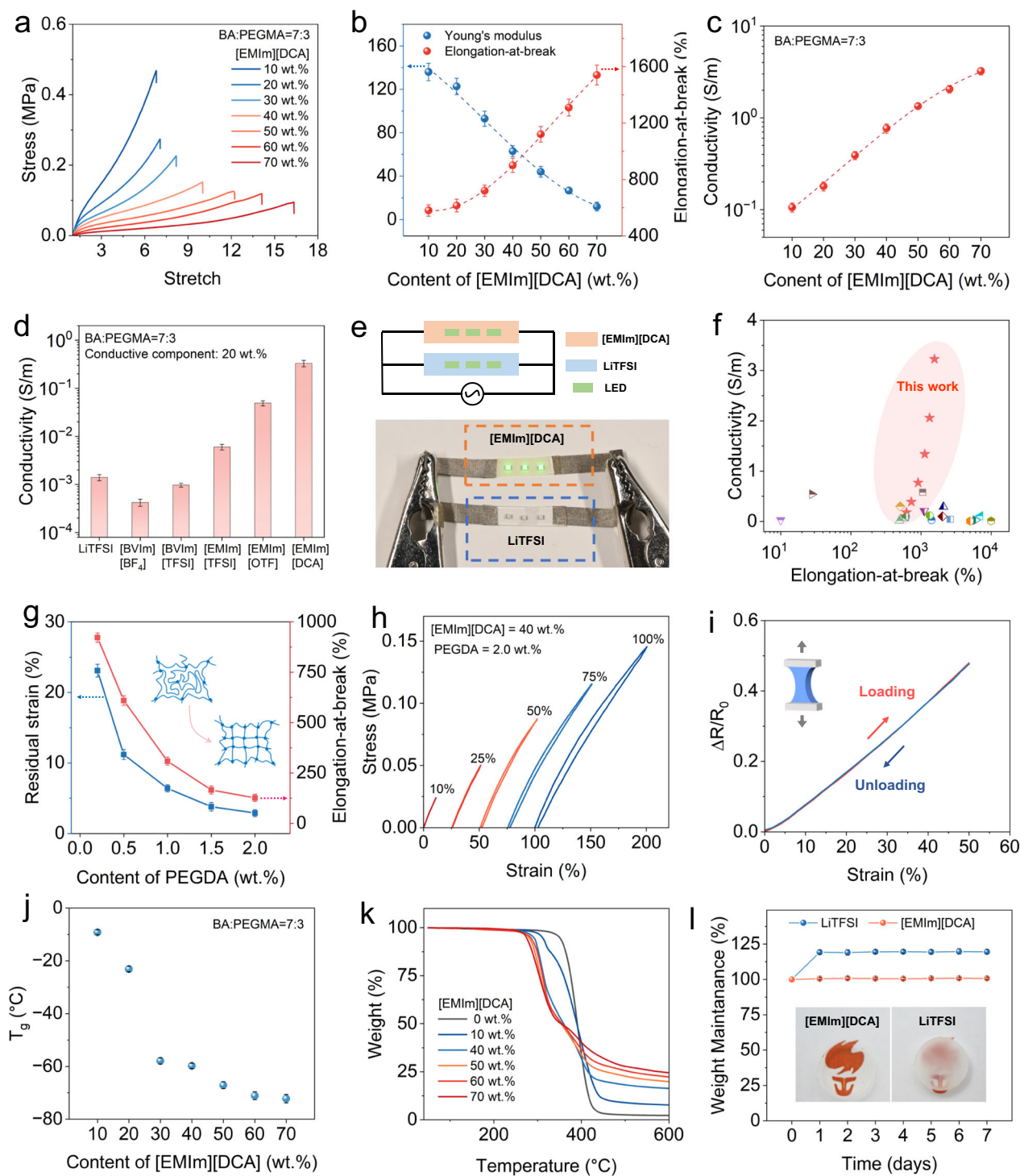
Fig. 2 | Thermomechanical and electrical properties of the CSN ionogel.
a Stress–strain behavior of the CSN ionogel with different [EMIm][DCA] contents.
b Effect of [EMIm][DCA] content on Young's modulus and elongation-at-break of the CSN ionogels. **c** Effect of [EMIm][DCA] content on conductivity. **d** Ionic conductivity of the P(BA-*co*-PEGMA) samples with different ionic conductive component. **e** Demonstration to compare the conductivity between the CSN ionogel with [EMIm][DCA] and the ionic conductor with LiTFSI. **f** Comparisons on conductivity and elongation-at-break between the CSN ionogel in this work and other reported ionogels. **g** Effect of PEGDA content on residual strain and elongation-at-break of the CSN ionogel. **h** Cyclic stress–strain curves at different maximum strains ranging from 10% to 100%. **i** Resistance responses of the CSN ionogel during a loading and unloading cycle with a maximum strain of 50%. **j** Effect of [EMIm][DCA] content on

glass transition temperature. **k** Thermogravimetric curves of the CSN ionogel with different [EMIm][DCA] contents. **l** Weight change of P(BA-*co*-PEGMA) samples with same content LiTFSI and [EMIm][DCA] in humid environments. The inset pictures were P(BA-*co*-PEGMA) samples with same content LiTFSI and [EMIm][DCA] after being stored at 20 °C and 80% humidity environment for 1 h. Data are presented as the mean values ± SD, $n = 3$ independent samples. Source data are provided as a Source Data file. 1-ethyl-3-methylimidazolium trifluoromethanesulfonate: [EMIm] [OTF]; 1-ethyl-3-methylimidazolium bis(trifluoromethylsulfonyl)imide: [EMIm] [TFSI]; 1-butyl-3-vinylimidazolium tetrafluoroborate: [BVIm][BF$_4$]; 1-butyl-3-vinylimidazolium bis((trifluorompropyl)sulfonyl)imide: [BVIm][TFSI]; Lithium bis(trifluoromethane sulfonimide): LiTFSI.
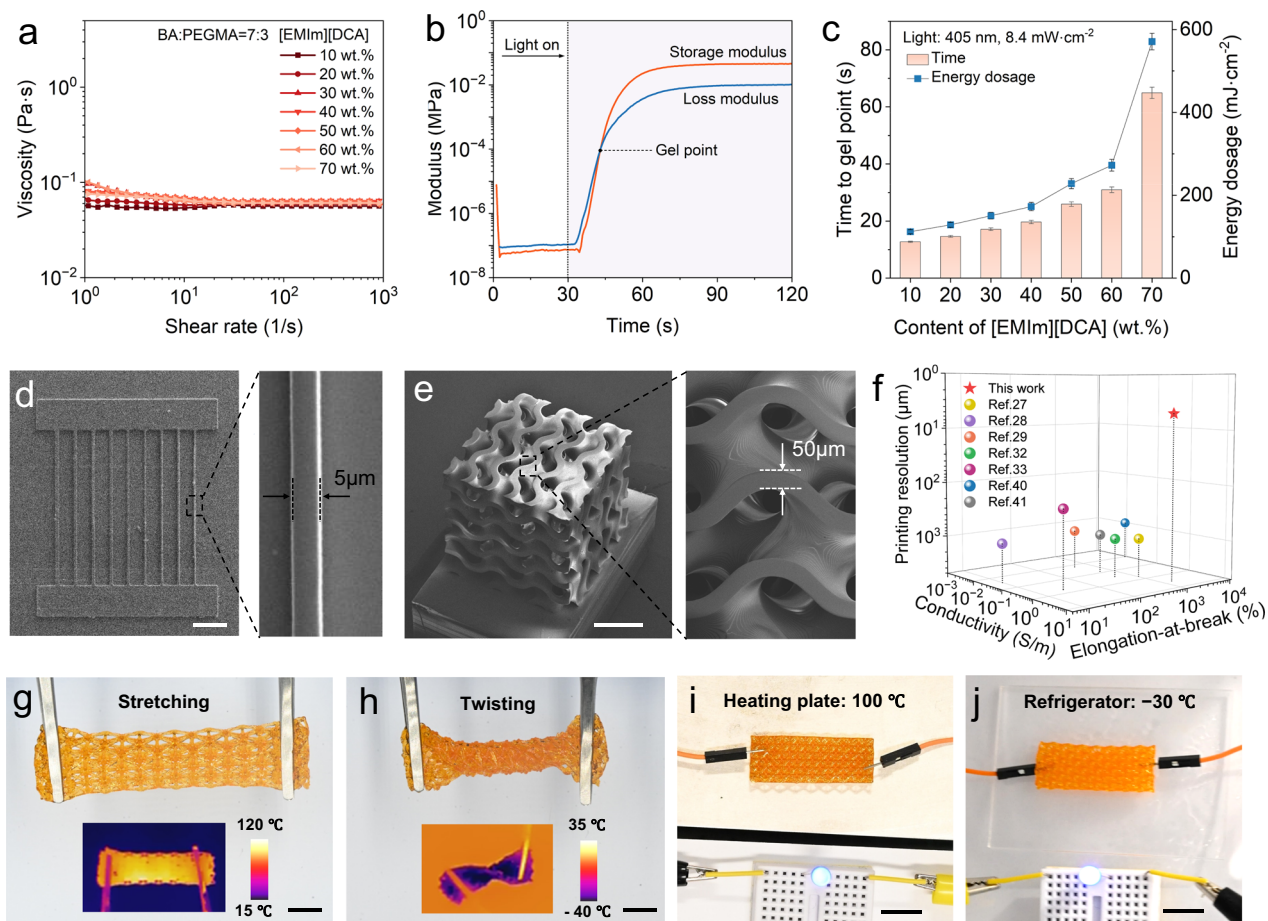
Fig. 3 | 3D printing of CSN ionogels. a Viscosity of CSN ionogel precursor solution versus content of [EMIm][DCA]. **b** Photorheological test to identify the gel point of the CSN ionogel. **c** Effect of [EMIm][DCA] content on time and energy dosage to gel point of the CSN ionogel. **d** SEM image of a 3D printed ionogel sample with ultrathin horizontal width. Scale bar: 100 μm. **e** SEM image of a Gyroid structure printed with CSN ionogel. Scale bar: 500 μm. **f** Comparisons on printing resolution, conductivity, and elongation-at-break between the CSN ionogel in this work and other reported 3D printing ionogels. **g**, **h** The lattice structure printed with CSN ionogel is highly deformable at (**g**) 100 °C and (**h**) −30 °C, respectively. Scale bar: 10 mm. **i**, **j** The lattice structure printed with CSN ionogel exhibiting good electrical conductivity at (**i**) 100 °C and (**j**) −30 °C, respectively. Scale bar: 10 mm. Data are presented as the mean values ± SD, $n = 3$ independent samples. Source data are provided as a Source Data file.

ionogels, CSN ionogel has high printing resolution without sacrificing stretchability and electrical conductivity[27–29,32,33,40,41] (Table S1). Furthermore, the 3D printed structures with the CSN ionogel exhibit high deformability and high conductivity in a wide temperature range. As shown in Fig. 3g and h, the 3D printed Octet truss structure is highly deformable at both 100 °C and −30 °C. The high conductivity of the Octet truss structure is maintained at both high (100 °C in Fig. 3i) and low temperatures (−30 °C in Fig. 3j).

Working mechanism of the 3D printed capacitive sensor with CSN ionogels

Due to high ionic conductivity, the CSN ionogel can be used to form electron double layer (EDL) capacitor with high capacitance. As illustrated in Fig. 4a, unlike conventional parallel-plate capacitor, the EDL capacitor substitutes the dielectric layer with ionic conductor sandwiched between two metal-based electrodes[16]. EDLs are generated at the interfaces between metal-based electrode and ionic conductor[51]. When voltage is applied, positive or negative charges on two electrodes attract ions with opposite polarity in the ionic conductor to form numerous electron-ion pairs. The separation distance between electron and ion is at nanometer scale. Thus, the electron-ion pairs generate numerous microscale capacitors with ultrahigh capacitance per unit area, which is up to around 10^3 times higher than that of parallel-

plate capacitors[22]. When an external force is applied, the contact area between ionic conductor and electrode increases significantly so that more electron-ion pairs are aggregated at interfaces to cause a dramatic increase in the capacitance.

As shown in Fig. 4b, we measure relative capacitance change ($\Delta C/C_0$) over applied pressure P to characterize the sensing properties of the CSN ionogel-based EDL sensor ([EMIm][DCA] content: 40 wt.%) and the parallel-plate counterpart ([EMIm][DCA] content: 0 wt.%). Here, ΔC is the change of capacitance, and C_0 is the initial capacitance without exerted pressure. The CSN ionogel-based EDL capacitive sensor exhibits significantly higher sensitivity S ($S = (\delta\Delta C/C_0)/\delta P$) which is 0.23 kPa^{-1} within the pressure range of 1−5 kPa. In contrast, the sensitivity of the parallel-plate capacitive sensor is only 0.016 kPa^{-1} under the same pressure range. Moreover, as shown in Fig. 4c, the parallel-plate capacitive sensor exhibits low initial and maximum capacitances ($C_0 = 2.7$ pF, $C_{max} = 4.1$ pF). Contrarily, due to the formation of EDL, the CSN ionogels capacitive sensor with 40 wt.% [EMIm][DCA] exhibits ultrahigh capacitance ($C_0 = 36.8$ nF, $C_{max} = 329.7$ nF), which are up to approximately four to five orders of magnitude higher than that of the parallel-plate capacitor. Furthermore, C_0 and C_{max} of the CSN ionogels capacitive sensor increase by increasing the [EMIm][DCA] content as more IL modules lead to more electron−ion pairs at the ionogel-electrode interface. Details can be found in Fig. S16. In the
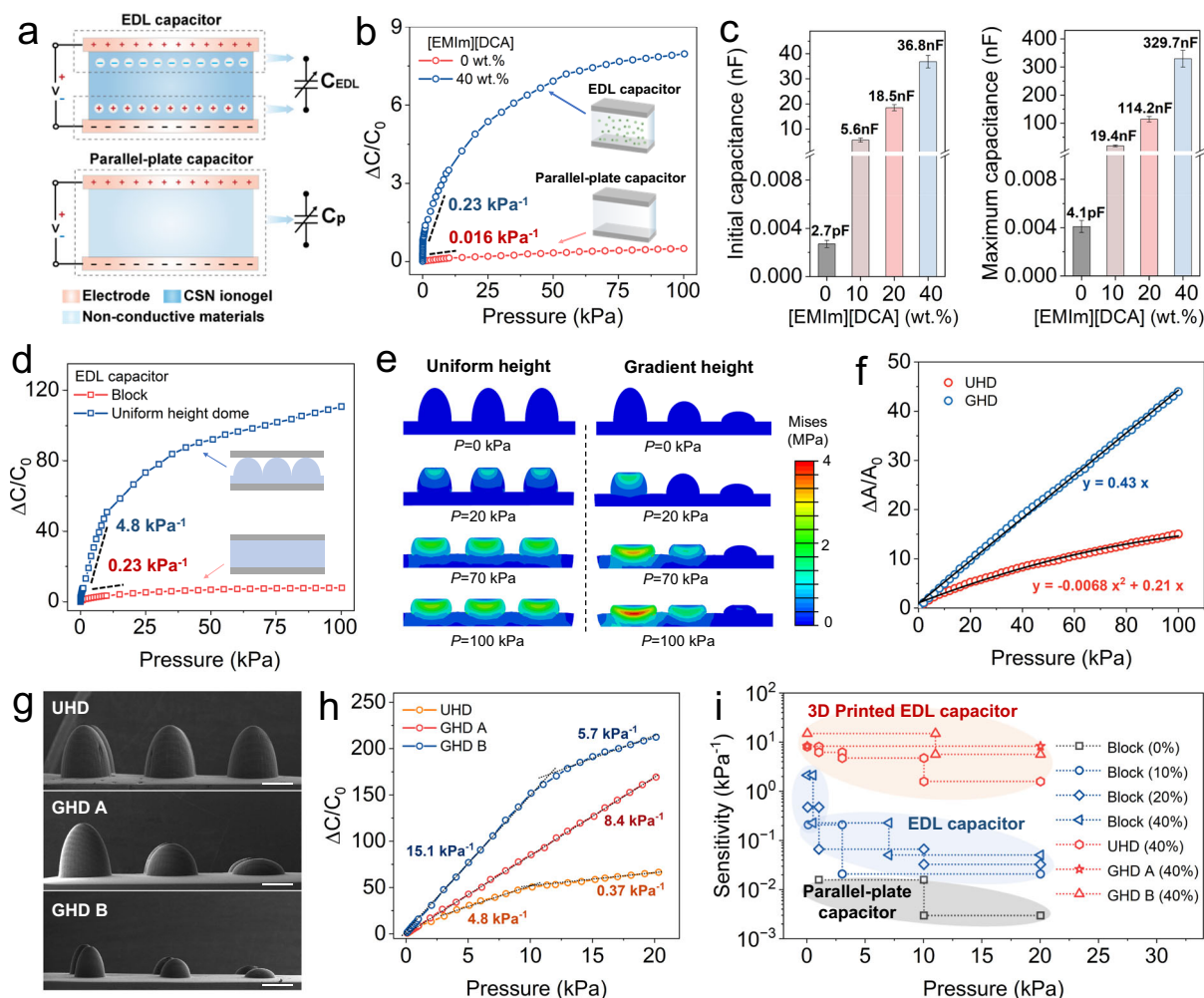
Fig. 4 | Design and the sensing mechanism of the 3D printed capacitive sensor based on CSN ionogels. a Sensing mechanisms of the parallel-plate capacitor (top) and the CSN ionogel-based EDL capacitor (bottom). **b** Comparison on the $\Delta C/C_0 - P$ relation between the parallel-plate capacitor and the CSN ionogel-based EDL capacitor. **c** Comparisons on initial capacitance (under no external pressure) and maximum capacitance (under the pressure of 100 kPa) between the parallel-plate capacitor and the CSN ionogel-based EDL capacitors with different [EMIm][DCA] contents. **d** Comparisons on the $\Delta C/C_0 - P$ relation of the 3D printed EDL capacitive sensors with block and dome-shaped CSN ionogel layers. **e** FEA simulation results

for pressing the domes with uniform height and gradient height. **f** Comparisons on the $\Delta A/A_0 - P$ relation between the three domes with uniform height and gradient height. **g** SEM images of the dome shaped CSN ionogels with uniform height and gradient height in different scales. Scale bar: 300 μm. **h** Comparison on the $\Delta C/C_0 - P$ relation of the CSN ionogel capacitive sensors with the corresponding micro-architectures from (**g**). **i** Performance comparison on the sensitivity of the different capacitive sensors in this work. Data are presented as the mean values ± SD, n = 3 independent samples. Source data are provided as a Source Data file.

following of this work, the CSN ionogels with 40 wt.% [EMIm][DCA] are used to form the EDL capacitive sensors unless otherwise specified.

High printability of the CSN ionogels allows us to fabricate them with intricate geometries, which can be used to further enhance the capacitance of the EDL capacitive sensors by changing the contacting process between CSN ionogel layer and metal-based electrodes. As shown in Fig. 4d, the sensitivity of the EDL capacitive sensor with the CSN ionogel layer printed in the dome shape is 4.8 kPa⁻¹ which is about 20 times higher than that of the EDL capacitive sensor with the block CSN ionogel layer. We can further tune the sensitivity and even linearity of the EDL capacitive sensor by printing the domes with gradient heights. Figure 4e presents the finite element analysis (FEA) results that compare the compressive process of three CSN ionogel domes with uniform and gradient heights. Details on FEA can be found in Materials and Methods. As compression proceeds, three domes with uniform height are compressed simultaneously, and the incompressible area (high stress area) gradually propagates through all the dome structures. In contrast, for the domes with gradient heights, when the tall dome becomes nearly incompressible, the medium dome starts to be

compressed; finally, the short dome begins to support load when the two taller domes are nearly incompressible. In Fig. 4f, the FEA simulations compare the $\Delta A/A_0 - P$ relations between the two designs. For the three domes with uniform height, the $\Delta A/A_0 - P$ relation (the UHD curve) exhibits apparent nonlinearity where the slope of the curve decreases as the pressure increases. In contrast, the gradient height imparts a linearity to the $\Delta A/A_0 - P$ relation (the GHD curve). As presented in Fig. S17, FEA simulations analyze the contact area contributions from the three domes. The medium and short domes start to contribute contact area when the pressure is greater than 20 kPa and 70 kPa respectively. Although the $\Delta A/A_0 - P$ relations from each individual domes are nonlinear, the combined effect exhibits linearity. Furthermore, as shown in Fig. 4g, we print dome-shape CSN ionogel structures with uniform and gradient heights. Figure 4h presents the $\Delta C/C_0 - P$ relations from the EDL capacitive sensors with the dome-shaped CSN ionogel layers shown in Fig. 4g. Compared with the sensor with uniform-height domes (UHD), the one with gradient-height domes (GHD A) exhibits a liner $\Delta C/C_0 - P$ relation with higher sensitivity of 8.4 kPa⁻¹ in a wide range (0 - 20 kPa). Moreover, we can further
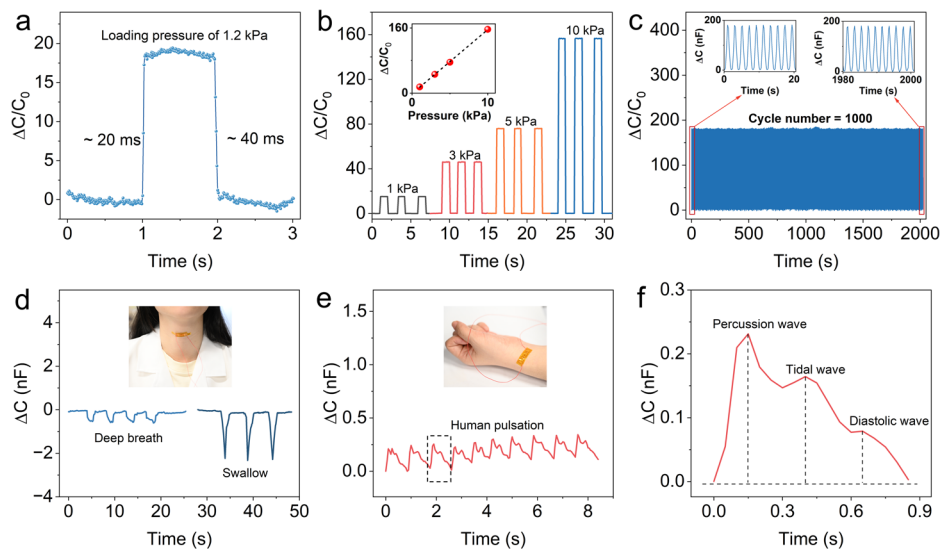
Fig. 5 | Sensing performance of the 3D printed capacitive sensor with CSN ionogels. a Instant response of the 3D printed capacitive sensor. **b** Capacitance response of the sensor under periodic loading pressures of 1, 3, 5, and 10 kPa, respectively. **c** Working stability of the sensor tested under 1000 cycles of 14 kPa pressure. The insets show the first 20 cycles and the last 20 cycles. **d** Real-time monitoring of human deep breath and swallow, respectively. The inset shows the pressure sensor attached to the throat. **e** Real-time monitoring of human pulsation. The inset shows the pressure sensor attached to the wrist. **f** A single pulse wave from the wrist, consisting of three characteristic peaks.

scale down the size of gradient-height domes in a factor of 0.6 (GHD B) to increase the sensitivity to 15.1 kPa^{-1} while keeping a good linearity in the pressure range from 0 to 12 kPa. Overall, as summarized in Fig. 4i, all the CSN ionogels-based EDL capacitive sensors display overall greater sensitivity over a larger range of applied pressure than that of the parallel-plate capacitive sensors. The sensing capability can be further improved by printing dome-shaped CSN ionogel layers.

Comprehensive characterization of the sensing performance

Next, we evaluate other critical properties of the 3D printed capacitive sensors with CSN ionogels. To evaluate the dynamic response speed of the sensor, we gently place a 3 g weight (equivalent pressure ~1.2 kPa) onto the sensor, and then quickly remove it. As shown in Fig. 5a, the sensor detects the variation in capacitance within 20 ms, and the capacitance returns to the initial value within 40 ms. Moreover, when we apply repeating stepwise pressures with different magnitudes (1, 3, 5, and 10 kPa), as found in Fig. 5b, our 3D printed EDL capacitive sensor presents reliable pressure-responsive capability, and a high linearity between applied pressure and variation in capacitance (inset of Fig. 5b). We further conduct cyclic loading test to evaluate the sensor's mechanical durability which also plays a crucial role for sensors under long-time or cyclic use. As shown in Fig. 5c, after 1000 cycles of loading and unloading at 14 kPa, the sensor shows no drift or fluctuation, confirming its high mechanical durability. Tiny pressures could be detected by the 3D printed EDL capacitive sensor owing to its high sensitivity. As shown in Fig. 5d, the 3D printed sensor can monitor and distinguish different types physiological signals (e.g., deep breath and swallow) of human larynx in real time. In addition, Fig. 5e shows that the 3D printed sensor is attached on human wrist to record real-time pulse signals (Movie S1). Figure 5f presents the magnified plot of the recorded human pulse wave where the three typical main waves (percussion-wave, tidal-wave, and diastolic-wave) can be clearly distinguished. These results demonstrate the potentials of the 3D printed EDL capacitive sensor in the applications of wearable pressure-sensing devices for healthcare monitoring and clinical diagnosis.

Robotic hand-sensor integration and multiplex sensing arrays

Integrated with 3D printed sensors, robotic hands can realize the tactile perception as humans and interact with the environment. As shown in Fig. 6a, we integrate the CSN ionogel-based EDL capacitive sensor onto a robotic gripper. When the grippers grasp an object, the sensor collects real-time capacitance variation (Fig. S18). Since the CSN ionogels exhibit high deformability and high conductivity under extreme conditions (Fig. 3 g–j), the CSN ionogel-based EDL capacitive sensor can detect pressure signals in a wide temperature range. As demonstrated in Fig. 6b, the robotic gripper picks up a metal block (weight: 62.58 g) at 25, 150 and -30 °C, respectively. At these three different temperatures, the CSN ionogel-based EDL capacitive sensor responses in a nearly same way in terms of the magnitude of capacitance variation, response speed, and repeatability (Movie S2). In Fig. 6c, a robotic gripper is integrated with an array of five CSN ionogel-based EDL capacitive sensors. When the grippers grab different objects with different geometries and weight such a toy duck (weight: 10.67 g in Fig. 6d), a centrifuge tube with water (weight: 35.24 g in Fig. 6e), and a table tennis ball (weight: 2.9 g in Fig. 6f), the array of five sensors response differently in terms of signal combinations in the five channels and the magnitude of capacitance variations (Fig. S19 and Movie S3). Furthermore, owing to the high sensitivity and fast response speed, the CSN ionogel-based EDL capacitive sensors can be used to form pressure sensor array for high-resolution pressure mapping. Figure 6g illustrates the design of a pressure sensor array composed of 4 × 4 sensing units. Figure 6h presents the snapshot of a fabricated pressure sensor array with 16 pixels. The performance of the pressure sensor array is demonstrated in Fig. S20 and Movie S4. In Fig. 6i, when we place a plastic block (1 g) and two Allen bolts (8.1 g) onto different pixels of the pressure sensor array, the corresponding sensor responses instantaneously with the different capacitance variations according to the weight of the applied object. In Fig. 6k–n, we demonstrate the pressure sensor array's capability of recognizing contact patterns by placing two blocks with different bottom-side patterns onto the pressure sensor array. As clearly shown in Fig. 6l, n, the synchronous capacitance variations only occur on the unit sensors which are pressed by the bottom of the placed block. Moreover, since the pressure sensor array is flexible, it can be directly attached onto a
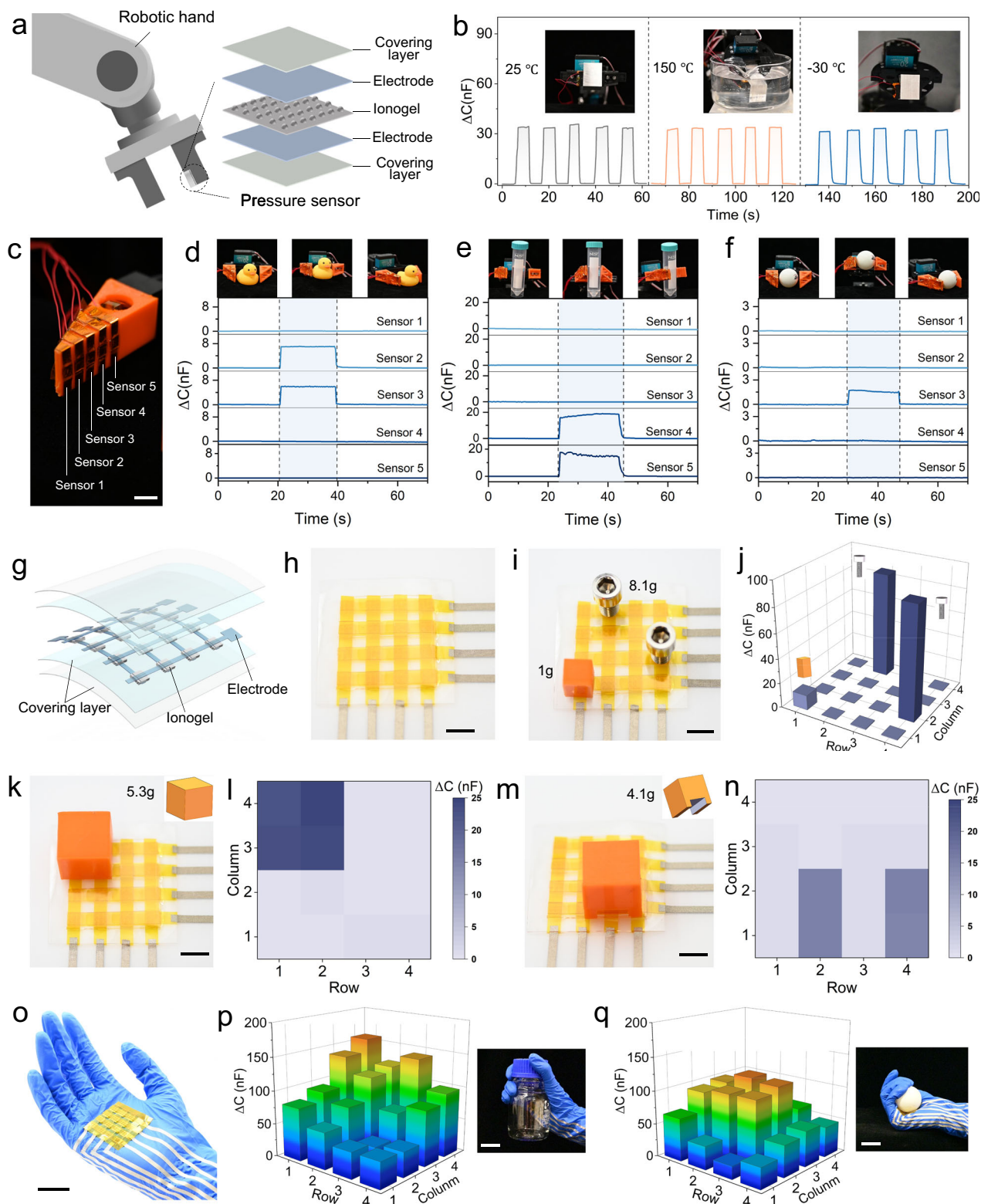
Fig. 6 | Robotic hand-sensor integration and multiplex sensing arrays.
a Schematic illustration for the robotic gripper integrated with a CSN ionogel-based EDL capacitive sensor. **b** Variation of capacitive signal during robotic hand holding a metal block (weight: 62.58 g) at 25, 150, and −30 °C. **c** Photograph of robotic hand integrated with a sensor array consisting of five CSN ionogel-based EDL capacitive sensors. Scale bar: 1 cm. **d**–**f** Real-time multichannel capacitance signals of the pressure sensors mounted on a robotic hand, corresponding to the operations of grabbing and releasing of a toy duck (**d**), a centrifuge tube filled with water (**e**), and a table tennis ball (**f**). **g** Schematic illustrations of the multiplex pressure sensor array. **h** Photograph showing the multiplex pressure sensor array with 4 × 4 sensing pixels. Scale bar: 10 mm. **i** Illustration of the top view of an integrated 4 × 4 sensor array loaded with a plastic block and two screws. **j** Corresponding signal mapping of (**i**). **k**–**n** Demonstration of the pressure sensor array's capability of recognizing contact patterns by placing two blocks with different bottom-side patterns onto the pressure sensor array. Scale bar: 10 mm. **o** Photograph showing multiplex pressure sensor array with 4 × 4 sensing pixels attached onto a glove. Scale bar: 20 mm. **p**, **q** The pressure distribution of a multiplex pressure sensor array on the glove, corresponding to grabbing of a bottle (**p**) and a table tennis ball (**q**). Scale bar: 20 mm.

human hand wearing a glove or a robotic hand (Fig. 6o). As a result, when the hand grasps different objects (a bottle in Fig. 6p, a table tennis ball in Fig. 6q), the pressure sensor array responses instantaneously to displace the corresponding contact pressure distributions (Fig. S21 and Movie S5).

Discussion

In this work, we develop the CSN ionogels for 3D printing capacitive sensors. We propose a photopolymerization-induced microphase separation strategy to prepare BA-PEGMA ionogel where PEGMA moieties form continuous microchannels that percolate in the polymer network to facilitate ion transportation. This strategy allows us to endow ionogels with high conductivity without sacrificing the printability and mechanical properties. The developed CSN ionogels exhibit high ionic conductivity, high stretchability, low degree of hysteresis, wide-temperature-range thermostability, and humidity tolerance. More importantly, due to the high compatible with DLP 3D printing, we can fabricate complex CSN ionogel micro-architectures with high resolution. We 3D print EDL capacitive sensors with superior sensing performances such as high sensitivity, high linearity, fast dynamic response, excellent cyclic stability, and wide operating temperature range. We make several demonstrations to exhibit the superior sensing performance of the 3D printed sensors. We use the printed sensor to monitor the real-time human deep breath and swallow, as well as pulsation. We integrate the printed sensors onto a robotic gripper which can sense grasping signals in a wide temperature range from -30 °C to 150 °C, and collect different combination of signals while grasping various objects. We further build a pressure sensor array composed of 4 × 4 printed sensors for real-time high resolution pressure mapping. The proposed CSN ionogels pave an efficient way to manufacture ionogel-based capacitive sensors with enhanced performances.

Methods

Materials

Benzyl acrylate (BA), 2,4,6-trimethylbenzoyl diphenylphosphine oxide (TPO), and lithium bis(trifluoromethane sulfonimide) (LiTFSI) were purchased from Shanghai Bide (China). Poly(ethylene glycol) methyl ether methacrylate (PEGMA, M_n = 950/500/300), methanol, Sudan I, 1-ethyl-3-methylimidazolium dicyanamide ([EMIm][DCA]), 1-ethyl-3-methylimidazolium trifluoromethanesulfonate ([EMIm][OTF]), 1-ethyl-3-methylimidazolium bis(trifluoromethylsulfonyl)imide ([EMIm][TFSI]), 1-butyl-3-vinylimidazolium tetrafluoroborate ([BVIm][BF$_4$]), and 1-butyl-3-vinylimidazolium bis((trifluorompropyl)sulfonyl)imide ([BVIm][TFSI]) were purchased from Shanghai Aladdin (China). Poly(ethylene glycol) diacrylate (PEGDA, M_n = 700) and hydroiodic acid (HI, 57 wt.%) were purchased from Sigma-Aldrich (China). All chemicals were used as received without further purification.

Characterizations

The transparency of ionngels (thickness ~1 mm) was evaluated using a UV-visible spectrophotometer (Lambda 950, PerkinElmer Inc., USA). Mechanical tests were conducted on MTS uniaxial tensile testing machine (MTS Criterion, Model 43.104 Dimensions, USA). The ionic conductivities were obtained by electrochemical impedance spectra, which were collected on an electrochemical workstation (CHI660E, Shanghai Chenhua Instrument Co., L., China). The capacitance and resistance were measured by using an LCR meter in a frequency of 1 kHz with a 1 V AC signal (TH2838H, Changzhou Tonghui Electronic Co., Ltd., China). Thermogravimetric Analysis (TGA) measurements were performed on a thermal gravimetric analyzer (TG 209F1, Netzsch Instruments Inc., Germany) via a scanning rate of 10 °C/min under flowing N$_2$. The glass transition temperature (T_g) of ionogels was measured with a dynamic mechanical analyzer (Q850, TA instruments Inc., USA) at a cooling rate of −3 °C/min. The viscosity of all ionogels

samples was measured by using a rheometer (DHR3, TA instruments Inc., USA) with a parallel plate geometry (diameter 20 mm, gap 200 μm). The gel point of all ionogels samples was measured by rheometer (DHR3, TA instruments Inc., USA) with a parallel plate geometry (diameter 20 mm, gap 100 μm). To perform these experiments, a UV light source (405 nm, 8.4 mW/cm^2) was attached to the rheometer. The FTIR spectra were recorded using an FTIR spectrophotometer (Thermo Nicolet iS50) from 400 to 4000 cm^{-1}.

Fabrication of CSN ionogel

CSN ionogels were fabricated by photopolymerization. First, PEGDA, photoinitiator TPO, and [EMIm][DCA] were dissolved in BA − PEGMA mixture, forming a transparent precursor solution. The compositions of the various ionogels are shown in Table S2-S6. Then, the solution was injected into a polytetrafluoroethylene mold. All ionogels were cured in 5 min by ultraviolet light irradiation.

3D Printing

The structures in Figs. 3d, 3e and Supplementary Fig. 15a were printed using a commercial 3D printer (nanoArch S130, BMF Precision Technology Co., China). The structures in Fig. 3g–j and Supplementary Fig. 15b were printed using a commercial 3D printer (nanoArch S240, BMF Precision Technology Co., China). All the EDL capacitive sensors (thickness: 700 μm, area: 0.25 cm^2) in Figs. 4–6 and Supplementary Figs. 16, 18–21 were printed using a commercial 3D printer (nanoArch S240, BMF Precision Technology Co., China).

Small-angle X-ray scattering (SAXS)

SAXS measurements were performed using X-rays with a wavelength (λ) of 1.54189 Å yielding scattering wavevectors q ($q = 4\pi \sin(\theta/2)/\lambda$, where θ is the scattering angle) in the range of 0.041–1.22 nm^{-1} (SAXSess mc2, Bruker Inc., Germany). Two-dimensional scattering data were azimuthally integrated to obtain one-dimensional intensity, I, versus q profiles.

Scanning electron microscopy (SEM)

PEGMA and IL domains of the ionogel were etched to create contrast for direct observation of the morphology via SEM. Following an established etching procedure, chunks of the ionogels monolith were immersed in an aqueous solution of 57 wt.% hydroiodic acid at 60 °C for 5 days, removed and rinsed in methanol, and dried in an oven for 30 h. The freeze-fractured surface of the SEM sample was sputter-coated with platinum and was imaged at an accelerating voltage of 5 kV (Apreo2 S Lovac, Thermo Fisher Scientific Inc., USA).

Finite element analysis (FEA)

To predict the deformation of the dome structures, FEA simulations were conducted by using the commercially available software package ABAQUS (V6.14, Dassault Systèmes Simulia Corp., USA). We use the Ogden hyperelastic model with strain energy density function to describe the nonlinear material behavior of ionogel. The material coefficients were set as μ_1 = 20.934 MPa, α_1 = 1.745, and D1 = 0.001 MPa, which were obtained by fitting the uniaxial tensile experiments of ionogel. The 3D model of the dome structures was constructed and analyzed on ABAQUS/Explicit (Simulia, Dassault Systemes). Solid tetrahedron linear element (element type C3D8H) was used to mesh the structures. The displacement was applied to the rigid plate above the dome structures to simulate the quasi-static compression.

Human participant recruitment

Informed consent was given by each human subject and all experiments were conducted under approval from the Institutional Review Board at the Southern University of Science and Technology under the protocol number 20240249. The participants (age range 20–30 years)

were recruited from SUSTech campus through advertisement by posted notices.

Statistics and reproducibility

All experiments were repeated independently with similar results for at least three times.

Reporting summary

Further information on research design is available in the Nature Portfolio Reporting Summary linked to this article.

Data availability

The data generated in this study are provided in the main article, Supplementary Information and Source data file. Source data are provided with this paper. Source data https://doi.org/10.6084/m9.figshare.26316862.

References

1. Sun, J. Y., Keplinger, C., Whitesides, G. M. & Suo, Z. Ionic skin. *Adv. Mater.* **26**, 7608–7614 (2014).
2. Keplinger, C. et al. Stretchable, transparent, ionic conductors. *Science* **341**, 984–987 (2013).
3. Yang, C. H. et al. Ionic cable. *Extrem. Mech. Lett.* **3**, 59–65 (2015).
4. Kim, C.-C., Lee, H.-H., Oh, K. H. & Sun, J.-Y. Highly stretchable, transparent ionic touch panel. *Science* **353**, 682–687 (2016).
5. Larson, C. et al. Highly stretchable electroluminescent skin for optical signaling and tactile sensing. *Science* **351**, 1071–1074 (2016).
6. Kim, H. J., Chen, B. H., Suo, Z. G. & Hayward, R. C. Ionoelastomer junctions between polymer networks of fixed anions and cations. *Science* **367**, 773–776 (2020).
7. Kim, Y. M., Kwon, J. H., Kim, S., Choi, U. H. & Moon, H. C. Ion-cluster-mediated ultrafast self-healable ionoconductors for reconfigurable electronics. *Nat. Commun.* **13**, 3769 (2022).
8. Schroeder, T. B. H. et al. An electric-eel-inspired soft power source from stacked hydrogels. *Nature* **552**, 214–218 (2017).
9. Ge, Q. et al. 3D printing of highly stretchable hydrogel with diverse UV curable polymers. *Sci. Adv.* **7**, eaba4261 (2021).
10. Shi, L. et al. Highly stretchable and transparent ionic conducting elastomers. *Nat. Commun.* **9**, 2630 (2018).
11. Cao, Y. et al. Self-healing electronic skins for aquatic environments. *Nat. Electron.* **2**, 75–82 (2019).
12. Pu, X. et al. Ultrastretchable, transparent triboelectric nanogenerator as electronic skin for biomechanical energy harvesting and tactile sensing. *Sci. Adv.* **3**, e1700015 (2017).
13. Wei, J. J. et al. Dissolution-crystallization transition within a polymer hydrogel for a processable ultratough electrolyte. *Adv. Mater.* **31**, 1900248 (2019).
14. He, X. N. et al. Multimaterial three-dimensional printing of ultraviolet-curable ionic conductive elastomers with diverse polymers for multifunctional flexible electronics. *ACS Appl. Mater. Interfaces* **15**, 3455–3466 (2023).
15. Lee, Y. et al. Triboresistive touch sensing: grid-free touch-point recognition based on monolayered ionic power generators. *Adv. Mater.* **34**, 2108586 (2022).
16. Bai, N. N. et al. Graded intrafillable architecture-based iontronic pressure sensor with ultra-broad-range high sensitivity. *Nat. Commun.* **11**, 209 (2020).
17. Bai, N. et al. Graded interlocks for iontronic pressure sensors with high sensitivity and high linearity over a broad range. *ACS Nano* **16**, 4338–4347 (2022).
18. Cheng, Y. et al. Aquatic skin enabled by multi-modality iontronic sensing. *Adv. Funct. Mater.* **32**, 2205947 (2022).
19. Bai, N. N. et al. A robotic sensory system with high spatiotemporal resolution for texture recognition. *Nat. Commun.* **14**, 7121 (2023).
20. Su, Q. et al. A stretchable and strain-unperturbed pressure sensor for motion interference-free tactile monitoring on skins. *Sci. Adv.* **7**, eabi4563 (2021).
21. Niu, H. S. et al. Perception-to-cognition tactile sensing based on artificial-intelligence-motivated human full-skin bionic electronic skin. *Adv. Mater.* **34**, 2202622 (2022).
22. Amoli, V. et al. A bioinspired hydrogen bond-triggered ultrasensitive ionic mechanoreceptor skin. *Nat. Commun.* **10**, 4019 (2019).
23. Huang, J., Yu, Z. & Wu, P. 3D printing of ionogels with complementary functionalities enabled by self-regulating ink. *Adv. Sci.* **10**, 2302891 (2023).
24. Chen, L. & Guo, M. Highly transparent, stretchable, and conductive supramolecular ionogels integrated with three-dimensional printable, adhesive, healable, and recyclable character. *ACS Appl. Mater. Interfaces* **13**, 25365–25373 (2021).
25. Cheng, J. X. et al. Centrifugal multimaterial 3D printing of multifunctional heterogeneous objects. *Nat. Commun.* **13**, 7931 (2022).
26. Zhang, B. et al. Mechanically robust and UV-curable shape-memory polymers for digital light processing based 4D printing. *Adv. Mater.* **33**, 2101298 (2021).
27. Wang, Z. et al. 3D printable, highly stretchable, superior stable ionogels based on poly(ionic liquid) with hyperbranched polymers as macro-cross-linkers for high-performance strain sensors. *ACS Appl. Mater. Interfaces* **13**, 5614–5624 (2021).
28. Lee, K. et al. 3D printing nanostructured solid polymer electrolytes with high modulus and conductivity. *Adv. Mater.* **34**, 2204816 (2022).
29. Yu, Z. L. et al. Transparent, mechanically robust, adhesive, temperature-tolerant, and 3D printable nanocomposite ionogels for flexible sensors. *ACS Appl. Mater. Interfaces* **15**, 51833–51845 (2023).
30. Melodia, D. et al. 3D printed solid polymer electrolytes with bicontinuous nanoscopic domains for ionic liquid conduction and energy storage. *Small* **19**, e2206639 (2023).
31. Zhang, J. et al. 3D Printable, ultra-stretchable, self-healable, and self-adhesive dual cross-linked nanocomposite ionogels as ultra-durable strain sensors for motion detection and wearable human-machine interface. *Chem. Eng. J.* **431**, 133949 (2022).
32. Ma, C. A. et al. Highly processable ionogels with mechanical robustness. *Adv. Funct. Mater.* **33**, 2211771 (2023).
33. Ahmed, K., Naga, N., Kawakami, M. & Furukawa, H. Extremely soft, conductive, and transparent ionic gels by 3D optical printing. *Macromol. Chem. Phys.* **219**, 1800216 (2018).
34. Rubinstein, M. & Colby, R. H. *Polymer Physics* (Oxford University Press, 2003).
35. Chopade, S. A., So, S. Y., Hillmyer, M. A. & Lodge, T. P. Anhydrous proton conducting polymer electrolyte membranes via polymerization-induced microphase separation. *ACS Appl. Mater. Interfaces* **8**, 6200–6210 (2016).
36. Schulze, M. W., McIntosh, L. D., Hillmyer, M. A. & Lodge, T. P. High-modulus, high-conductivity nanostructured polymer electrolyte membranes via polymerization-induced phase separation. *Nano Lett.* **14**, 122–126 (2014).
37. Chopade, S. A. et al. Robust polymer electrolyte membranes with high ambient-temperature lithium-ion conductivity via polymerization-induced microphase separation. *ACS Appl. Mater. Interfaces* **9**, 14561–14565 (2017).
38. Yoshida, Yukihiro, Baba, Osamu & Saito, G. Ionic liquids based on dicyanamide anion: Influence of structural variations in cationic structures on ionic conductivity. *J. Phys. Chem. B* **111**, 4742–4749 (2007).
39. Yu, Z. C. & Wu, P. Y. Underwater communication and optical camouflage ionogels. *Adv. Mater.* **33**, 2008479 (2021).
40. Lei, Z. Y. & Wu, P. Y. A highly transparent and ultra-stretchable conductor with stable conductivity during large deformation. *Nat. Commun.* **10**, 3429 (2019).

41. Yao, Y. et al. Granular ionogel particle inks for 3D printed tough and stretchable ionotronics. *Research* **6**, 0104 (2023).
42. Yiming, B. et al. Ambiently and mechanically stable ionogels for soft ionotronics. *Adv. Funct. Mater.* **31**, 2102773 (2021).
43. Shi, L. et al. Highly stretchable and transparent ionic conductor with novel hydrophobicity and extreme-temperature tolerance. *Research* **2020**, 1–10 (2020).
44. Xu, L. G. et al. A transparent, highly stretchable, solvent-resistant, recyclable multifunctional ionogel with underwater self-healing and adhesion for reliable strain sensors. *Adv. Mater.* **33**, 2105306 (2021).
45. Zhang, M. W. et al. Mechanically robust and highly conductive ionogels for soft ionotronics. *Adv. Funct. Mater.* **33**, 2208083 (2023).
46. Shi, P. R., Wang, Y. F., Tjiu, W. W., Zhang, C. & Liu, T. X. Highly stretchable, fast self-healing, and waterproof fluorinated copolymer ionogels with selectively enriched ionic liquids for human-motion detection. *ACS Appl. Mater. Interfaces* **13**, 49358–49368 (2021).
47. Chen, T. et al. Highly conductive and underwater stable ionic skin for all-day epidermal biopotential monitoring. *Adv. Funct. Mater.* **32**, 2206424 (2022).
48. Cao, Y. et al. A transparent, self-healing, highly stretchable ionic conductor. *Adv. Mater.* **29**, 1605099 (2017).
49. Yoon, S. G., Koo, H.-J. & Chang, S. T. Highly stretchable and transparent microfluidic strain sensors for monitoring human body motions. *ACS Appl. Mater. Interfaces* **7**, 27562–27570 (2015).
50. Cao, Y., Chen, Y., Sun, X., Zhang, Z. & Mu, T. Water sorption in ionic liquids: kinetics, mechanisms and hydrophilicity. *Phys. Chem. Chem. Phys.* **14**, 12252–12262 (2012).
51. Liu, Q. X. et al. Highly transparent and flexible iontronic pressure sensors based on an opaque to transparent transition. *Adv. Sci.* **7**, 2000348 (2020).

Acknowledgements

Author contributions

X.H. and Q.G. conceived the ideas and designed the research. X.H. synthesized the materials and conducted the experiments. X.H., H.C., B.J., H.Y., K.D., and J.Z. demonstrated the applications. Q.L. helped the structural design and performed FEA simulations. J.C. and H.L. assisted 3D printing. X.H., B.Z., and Q.G. analyzed the data. X.H. drafted the manuscript. X.H., B.Z., and Q.G. revised the manuscript.

Competing interests

Q.G. and X.H. have applied a Chinese patent on this research (application number: 2024106328615) through Southern University of Science and Technology. The remaining authors declare no competing interests.

Additional information

Supplementary information The online version contains supplementary material available at https://doi.org/10.1038/s41467-024-50797-w.

Correspondence and requests for materials should be addressed to Qi Ge.

Peer review information *Nature Communications* thanks J Devin MacKenzie, Liliana Tomé, and the other, anonymous, reviewer(s) for their contribution to the peer review of this work. A peer review file is available.

Reprints and permissions information is available at http://www.nature.com/reprints

Publisher's note Springer Nature remains neutral with regard to jurisdictional claims in published maps and institutional affiliations.